Progress in Photovoltaics: Research and Applications

WILEY

PROGRESS IN PHOTOVOLTAICS

RESEARCH ARTICLE

A Spatially Resolved Evaluation of Accelerated Environmental Aging on Emerging Polypropylene-Based Photovoltaic Backsheets Using Raman Spectroscopy

Ashlee Aiello[1] | Stefan Mitterhofer[2] | Jan Obrzut[1] | Karissa L. Jensen[1] | Patryk Wąsik[3] | Chiara Barretta[4] | Gernot Oreski[4] | Stephanie S. Watson[1] | Lipiin Sung[1] | Xiaohong Gu[1]

[1]National Institute of Standards and Technology, Gaithersburg, Maryland, USA | [2]Foreign Associate, National Insitute of Standards and Technology, Gaithersburg, Maryland, USA | [3]National Synchrotron Light Source II, Brookhaven National Laboratory, Upton, New York, USA | [4]Polymer Competence Center Leoben, Leoben, Austria

Correspondence: Ashlee Aiello (ashlee.aiello@nist.gov) | Xiaohong Gu (xiaohong.gu@nist.gov)

Received: 23 September 2024 | **Revised:** 30 January 2025 | **Accepted:** 21 February 2025

Funding: This research used the Soft Matter Interfaces 12-ID beamline of the National Synchrotron Light Source II, a US Department of Energy (DOE) Office of Science User Facility operated for the DOE Office of Science by Brookhaven National Laboratory under contract no. DE-SC0012704.

Keywords: accelerated aging | backsheets | nanoindentation | photovoltaics (PVs) | polyolefin | polypropylene | Raman spectroscopy | reliability

ABSTRACT

Accelerated aging was used to assess environmental degradation in emerging co-extruded polypropylene (PP)-based backsheets under three different environmental conditions (65°C/20% relative humidity (RH), 75°C/20% RH, and 75°C/50% RH). Although differential scanning calorimetry did not measure crystallinity changes with exposure, spatially resolved Raman spectroscopy identified crystallinity increases in the core layer of aged samples, indicating a heterogeneous postcrystallization process. The Raman results were in agreement with synchrotron-based microfocused wide-angle X-ray scattering measurements. Cross-sectional nanoindentation was used to correlate localized crystallinity shifts with changes in Young's modulus. A similar trend was found where increased modulus was measured in the core layer, supporting the relationship between modulus and crystallinity. Finally, dielectric characterization was used to assess the impact of these material property changes on performance. While changes in the backsheet material properties and dielectric performance were observed with accelerated aging, these shifts generally equilibrated with time, indicating overall stability in response to environmental stressors. Additionally, the identified heterogeneous material property changes indicate that spatially resolved crystallinity measurements may be a valuable early failure indicator to be used in the assessment of PV backsheet long-term durability.

1 | Introduction

Photovoltaic (PV) backsheets play an important role in ensuring PV module reliability by providing environmental protection and electrical insulation. Early backsheet failure, such as the catastrophic cracking of polyamide-based backsheets which occurred in as little as 4 years [1–3] or severe inner layer cracking in polyethylene terephthalate (PET)-based backsheets [4], can result in dramatically reduced module lifetime. As such, it is critical that the underlying cause of failure mechanisms is fully identified, especially since standardized reliability testing does not always accurately reproduce real-world failure modes [5, 6]. This is difficult to achieve, however, due to the fact that many different types and combinations of interactions can serve as the cause of failure in PV backsheets, such as chemical degradation due to UV exposure, thermally

induced embrittlement, or interactions between different module components [6, 7].

Postcrystallization has been correlated with multiple material property changes in different PV backsheet systems, including embrittlement and chemical degradation [8, 9], making this a critical early failure indicator. Differential scanning calorimetry (DSC) is used as the industry standard measurement of polymer crystallinity, but this method is destructive and lacks spatial resolution. The multilayered structure of PV backsheets adds complexity to overall DSC data interpretation with changes isolated to thinner layers being extremely difficult or even impossible to measure. PV backsheets typically experience heterogeneous degradation and subsequent failure, requiring spatially resolved measurement techniques to identify the root cause of the degradation mechanism. Previous applications of Raman spectroscopy to PV modules have primarily been limited to encapsulant degradation [10–12] and the identification of individual components in unexposed backsheets [13, 14]. However, Raman spectroscopy can also be used to measure spatially resolved polymeric crystallinity along with chemical changes [15], which can offer unique advances towards the identification of degradation mechanisms and their underlying causes, along with early failure monitoring in heterogeneous PV backsheets. Specifically, this provides the opportunity to capture crystallinity changes that may be isolated to specific layers or regions within the backsheet structure. This information can play an important role in evaluating of new emerging backsheet materials as companies continue to introduce new alternatives in response to cost and design requirements.

Recently introduced co-extruded polypropylene (PP)-based backsheets have been identified as a promising alternative to traditional laminated PET-based backsheets. Bulk property and surface characterization of these multilayered backsheets after accelerated aging have indicated that these materials are generally stable and show minimal material property changes with environmental exposure [7, 16–18]. However, these characterization methods cannot capture localized shifts or changes isolated to the core layer. To more thoroughly assess the reliability of these emerging backsheets, accelerated environmental aging was performed under ultraviolet (UV) exposure using three sets of conditions—(1) 65°C/20% relative humidity (RH), (2) 75°C/20% RH, and (3) 75°C/50% RH. The cross-sectional crystallinity was measured using Raman spectroscopy and compared with traditional DSC. The spatially resolved crystallinity results were validated using synchrotron-based microfocused beam wide-angle X-ray scattering (WAXS), which can similarly provide spatially resolved crystallinity data. However, this method is considerably less accessible for industry use and cannot capture chemical changes. The cross-sectional crystallinity was also compared with spatially resolved Young's modulus, E, measurements to compare the correlation between crystallinity and mechanical property changes throughout each backsheet layer. We then go on to investigate the impact of crystallinity on dielectric performance using a novel, nondestructive, ultrasensitive microwave cavity measurement where the complex dielectric permittivity is measured at room temperature as a function of RH [19–21]. These results are discussed along with their implications regarding the long-term reliability of PP-based backsheets.

2 | Methods

2.1 | General

Equipment and material are identified in the article to adequately specify the experimental details. Such identification does not imply recommendation by the National Institute of Standards and Technology nor does it imply that the materials are necessarily the best available for the purpose.

2.2 | Sample Preparation

Co-extruded PP backsheets [7, 17, 18] were exposed to accelerated aging using the NIST Simulated Photodegradation via High Energy Radiant Exposure (SPHERE) [22], an integrated sphere-based device with a uniform high energy light source, as part of a previous study [18]. Samples were exposed to an averaged UV irradiance of 135 Wm^{-2} (295 to 400 nm, Figure S1) with the air side facing the exposure source for a total exposure of 1710 MJm^{-2} for each treatment condition. This exposure duration was chosen in support of the extended lifetime goal of 50-year modules set by the Department of Energy, as it is an approximate equivalent to 50 years of exposure in Arizona, assuming 10% albedo [18, 23]. Three different treatment conditions were used—(1) 65°C/20% RH, (2) 75°C/20% RH, and (3) 75°C/50% RH. Backsheet samples were cut and removed throughout exposure at 340 MJm^{-2} (30 days), 1110 MJm^{-2} (97 days), and 1710 MJm^{-2} (146 days). Cross-sections of each sample were then prepared by mounting in epoxy and using a gravity diamond saw to cut ≈ 20-μm-thick slices.

2.3 | Raman Characterization

Raman spectroscopy measurements were conducted using a Raman microscope (Senterra II, Bruker, Billerica, MA) with a 785-nm excitation wavelength, λ, at 50 mW focused through a 10× objective (0.3 numerical aperture, which corresponds to an approximate spot size of 3.2 μm for λ = 785 nm) and using a 50 μm × 1000 μm aperture. Four 20-s exposures with 4 cm^{-1} step size were averaged together to generate each spectrum. To provide spatial resolution, line scans measurements were completed using a 10-μm step size across the cross-sectioned backsheet beginning at the air-side layer. Five line scans were taken for each sample. Background subtraction was performed using OPUS software package (Bruker) using the concave rubberband algorithm, and further analysis was completed using OriginPro. The PP crystallinity, x_c, was measured according to the method outlined by Nielsen et al., where

$$x_c = \frac{I_{810}}{I_{810} + I_{830} + I_{842}} \times 100\,\% \tag{1}$$

and I_{810} is the integrated area of the crystalline 810 cm^{-1} peak, I_{830} is the integrated area of the amorphous 830 cm^{-1} peak, and I_{842} is the integrated area of the isomeric defect phase consisting of helical chains [24].

2.4 | DSC

DSC measurements were completed using Q2000 (TA Instruments, New Castle, DE). Approximately 5 mg of sample was used for each measurement, with the air side being placed face down into the Al hermetic pans. Samples were heated from −40°C to 300°C, cooled to −40°C, then heated again to 300°C at 10 K/min under N_2 flow (50 mL/min). Three measurements were taken for each reported condition. PP crystallinity, x_c, was calculated according to the method outlined by Nielsen et al., where

$$x_c = \frac{H}{H_0}\frac{\rho_a}{\rho_c}\left[1-\left(1-\frac{\rho_a}{\rho_c}\right)\right]\times 100\,\% \tag{2}$$

and $H_0 = 148\,Jg^{-1}$ is the heat of fusion for the PP crystal, $\rho_a = 0.85\,gcm^{-3}$ is the density of the amorphous state, and $\rho_c = 0.936\,gcm^{-3}$ is the density of the crystalline state [24].

2.5 | Nanoindentation

Cross-sections of the samples were prepared by potting in epoxy and cutting the surface with a diamond knife using a microtome (Leica Biosystems Nussloch GmbH, Nussloch, Germany). This cut ensures a flat, smooth surface as is required by nanoindentation (Nano Indenter G200, KLA, Milpitas, CA). Five lines of indents are then made on the cross-section using a 2-μm radius, 90° sphero-conical tip. The indentation depth is 2 μm; the distance between indents is 20 μm. The used indentation method is the continuous stiffness method, where an oscillating tip is indented into the material to extract the mechanical properties [25]. We focus on Young's Modulus, which is obtained from the flat areas of the depth-modulus curves [26].

2.6 | Laser Scanning Confocal Microscopy (LCSM)

Indents were visualized under a laser scanning confocal microscope using a Zeiss LSM800 (Carl Zeiss Microscopy, White Plains, NY) with a 50× objective. The locations of the individual indents and assignment to the corresponding layers are extracted from the LSCM images. The thickness of the individual layers is then measured in these cross-sectional images to evaluate any changes during degradation, for example, those due to shrinkage or erosion.

2.7 | Synchrotron-Based Microfocused WAXS

Synchrotron-based microfocused beam WAXS measurements were taken at the Soft Matter Interfaces (SMIs) Beamline (12-ID) of the National Synchrotron Light Source II (NSLS-II) at Brookhaven National Laboratory using a photon energy of 16.1 keV (wavelength = 0.7009 Å) and beam size of 2 μm × 25 μm (vertical × horizontal). Scattered intensity was measured using a Pilatus3 900 k-W (Dectris, Switzerland) detector positioned 280 mm from the sample. Scans were taken in 2-μm steps across the sample surface. The integrated (110) peak at 2.02 $Å^{-1}$ was used to estimate shifts in crystallinity across the cross-section following a linear background subtraction (Figure S2).

2.8 | Dielectric Characterization

Complex dielectric permittivity ($\varepsilon_r^* = \varepsilon_r' - j\varepsilon_r''$) measurements were carried out on PV backsheets samples at room temperature as a function of RH using a noncontact resonant microwave cavity method described in references [19–21]. The cavity testing fixture geometry dimensions follow the WR90 standard (127-mm length, rectangular waveguide [WR] 2.3 cm [0.90 in] internal width, and 10-mm internal vertical height). The waveguide is impedance terminated with near cross-polarized coaxial-to WR90 couplers on both sides, creating a standing wave, that is, resonance due to superposition of transmitted and reflected waves. The testing fixture is connected to a vector network analyzer (Agilent N5225A‡), which measures the transmission scattering parameter, S_{21}, of the resonant peak, the resonant frequency, f_x, and the half power bandwidth, Δf_x. The cavity operates at microwave frequencies, ($f_0 = 7.435$ GHz) in the transverse electric field mode ($TE_{1,0,3}$) where the electric field attains a maximum value at the cavity center.

Our previous studies [19–21] have shown that the classical perturbation model for a small specimen inside a rectangular cavity operating in the $TE_{1,0,n}$ resonant mode can be simplified to linear expressions:

$$y' = \left(\varepsilon_r' - 1\right)2x - b' \tag{3a}$$

$$y'' = \varepsilon_r''4x - 2b'' \tag{3b}$$

The real permittivity, ε_r', and the dielectric loss, ε_r'', can then be determined from the consequent slopes of Equation (3), where intercepts b' and b'' are constant. The parameters x, y', and y'' in Equation (3) are defined through the following relations:

$$x = \frac{V_x}{V_0}, y' = \frac{f_0 - f_x}{f_0}, \text{ and } y'' = 1/Q_x - 1/Q_0 \tag{4}$$

where f_0 and Q_0 are the resonant frequency and quality factor of the empty cavity having the volume V_0. Correspondingly, the values of f_x and Q_x then represent the resonant frequency and quality factor in the cavity with the specimen volume, V_x. The quality factor ($Q = f_r/\Delta f$) is a dimensionless parameter describing the ratio of energy stored in the resonant circuit to time-averaged power loss of the cavity or equivalently, a resonator's half power bandwidth (Δf) relative to the resonant frequency (f_r).

The cavity-testing fixture is mounted inside an environmental enclosure, enabling measurements under controlled RH atmosphere [21]. Prior to measurements, 8-mm width (w) and 20-mm height (h) samples were first conditioned inside the environmental encloser for 24 h at 1% RH at room temperature. During measurements, the specimen is inserted into the cavity through a small slot machined in the center of the cavity. Insertion of a specimen in volume steps ($V_x = wth_x$) causes the resonant peak to shift to lower frequencies f_x in proportion to ε_r', while the corresponding quality factor, $Q_x = f_x/\Delta f_x$, decreases in proportion to ε_r''. Δf_x is the resonator's half-power bandwidth, relative to the resonant frequency f_x. Typically, 40 pairs of data points, f_x and Q_x, are collected, while h_x increases in steps from 0 mm to $h_{max} = 10$ mm, where h_{max} is

the inner vertical dimension of the WR90 waveguide. This approach makes each step (i) equivalent to measurement of separate specimens of different volume V_x(i) exposed to the same RH atmosphere. The (f_x) and (Q_x) data points are then fitted to linear portion of Equation 3, where slope Equation (3a) corresponds to ε_r' and the slope of Equation (3b) corresponds to ε_r'' measured with typical uncertainty in ε_r' and ε_r'' of 10^{-4}.

3 | Results and Discussion

3.1 | Cross-Sectional Characterization

The PP backsheets are comprised of three layers with the bulk of the sample being formed by the core layer (≈ 224-μm thickness), as shown in Figure 1. Both outer layers reflect visible light more strongly compared with the core layer, but the air-side layer (≈ 27.7-μm thickness) is relatively flat in comparison with the cell-side layer (≈ 26.5-μm thickness), which shows substantial surface roughness. Figure 2 shows the comparison of Raman spectra of each layer, and Raman peak assignments are listed in Table 1. Strong rutile TiO_2 bands are measured at 236, 447, and 609 cm^{-1} in the outer layers that are absent from the core layer, which account for this increased visible light reflectivity. TiO_2 is a common backsheet additive pigment used to increase reflectivity and improve module performance [6]. The core layer shows less intense peaks at 401, 456, 528, and 678 cm^{-1} in this region, which are attributed to γ-Al_2O_3 [27]. The 401, 528, and 678 cm^{-1} peaks are also present in the air- and cell-side spectra, but the 456 and 621 cm^{-1} peaks are too low in intensity to be deconvoluted from the TiO_2 bands. The presence of γ-Al_2O_3 is consistent with X-ray photoelectron spectroscopy measurements of the air and cell side surfaces reported in an earlier study of these materials and may be a residual Ziegler-Natta catalyst from the PP synthetization process [18]. The same PP peaks are measured in all three layers, although the intensities of the crystalline 810 cm^{-1} (CH_2 rock, C–C stretch, C–CH_3 stretch), amorphous 842 cm^{-1} (CH_2 rock, C–CH_3 stretch), 1000 cm^{-1} (CH_3 rock, CH bend), 1154 cm^{-1} (C–C stretch, CH bend), and 2800 to 3000 cm^{-1} (CH stretch) peaks were higher for the core compared with the outer layers.

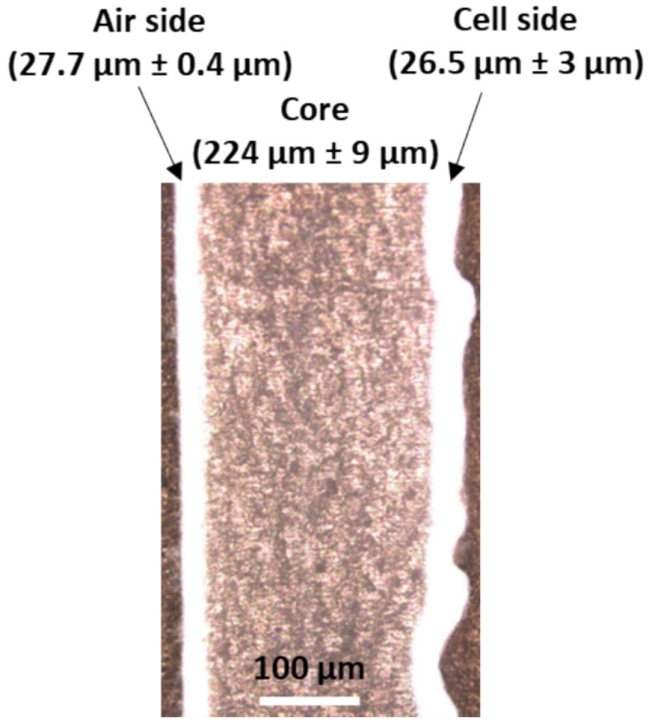

FIGURE 1 | Optical micrograph of a cross-sectioned as-received PP-based backsheet. [Color figure can be viewed at wileyonlinelibrary.com]

3.2 | Exposure Effects on Chemical Degradation

Accelerated environmental aging did not produce any notable peak shifting in the Raman spectra (Figures 3, S3, and S4), indicating general stability of the polymer with limited degradation product formation. The C–H stretch peak intensities in the 2800 to 3000 cm^{-1} region decreased after aging for all environmental conditions with a minimum intensity for 97 days of exposure (Figures 3, S3, and S4 [middle panel]), but this effect was limited to the core layer and was not observed in the air- and cell-side layers. Spatially resolved TiO_2 peak intensity shifts, calculated by the sum of the integrated 447 and 609 cm^{-1} peak areas, were measured with exposure where the TiO_2 peak intensity decreased in the 10 μm closest to the air side surface layer (Figure 4). For low humidity exposures (65°C/20% RH and 75°C/20% RH), the TiO_2 intensity increased towards the middle of the air side layer, possibly due to TiO_2 migration or rearrangement within the air side layer with exposure. Shifts in the TiO_2 intensity were also observed in the cell side layer, but the thickness variations in the cell side layer of the samples made a definitive trend difficult to identify. TiO_2 was not measured in the core layer, indicating that migration was limited to the outer layers. Other changes in peak intensity were measured but with no observable trend. For instance, the core layer of the backsheet aged at 75°C/20% RH showed an initial decrease in the

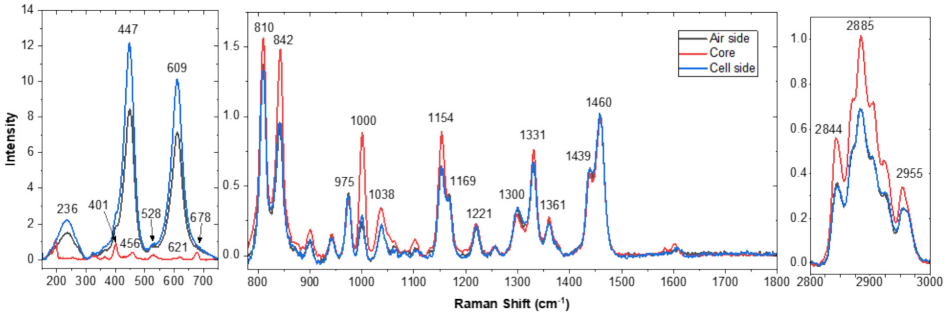

FIGURE 2 | Representative Raman spectra comparison of air-side, core, and cell-side layers in unexposed PP-based backsheets. Spectra are normalized to the 1460 cm^{-1} peak. [Color figure can be viewed at wileyonlinelibrary.com]

TABLE 1 | Raman peak assignments of PP-based backsheet [24, 27–34].

Raman shift (cm^{-1})			
Outer layers	**Core layer**	**Assignment**	**Reference**
236		Rutile TiO_2	[21, 22]
401	401	γ-Al_2O_3 (A_g)	[20]
447		Rutile TiO_2 (E_g)	[21–23]
	456	γ-Al_2O_3 (A_g)	[20]
528	528	γ-Al_2O_3 (A_g)	[20]
609		Rutile TiO2 (A_{1g})	[21–23]
	621	γ-Al_2O_3 (A_g)	[20]
678	678	γ-Al_2O_3 (A_g)	[20]
810	810	CH_2 rock, C–C stretch, C–CH_3 stretch	[14, 24–26]
842	842	CH_2 rock, C–CH_3 stretch	[24–26]
975	975	C–C stretch, CH_3 rock	[24–26]
1000	1000	CH_3 rock, CH bend	[24–26]
1038	1038	C–C stretch, C–CH_3 stretch	[25–27]
1154	1154	C–C stretch, CH bend	[14, 24–26]
1169	1169	C–C stretch, CH_3 rock	[24–26]
1221	1221	CH_2 twist, CH bend, C–C stretch	[24–26]
1300	1300	CH_2 wag, CH bend	[25, 26]
1331	1331	CH bend, CH_2 twist	[24, 26]
1361	1362	CH_3 bend, C–C stretch	[25, 26]
1439	1439	CH_2 bending	[14, 24, 25]
1460	1460	CH_2 bending, CH_3 asymmetric bending	[14, 24–26]
2844	2844	CH_2 symmetric C–H stretch	[26]
2885	2885	CH_3 symmetric C–H stretch	[26]
2955	2955	CH_3 asymmetric C–H stretch	[26]

1000 cm^{-1} peak intensity with exposure for the 30 and 97-day measurements, followed by a large increase after 146-day exposure. Similar inconsistencies were seen for the 65°C/20% RH (Figure S3) and 75°C/50% RH (Figure S4) conditions. Overall, these results suggest some minor degradation within the core layer with general overall chemical stability of the backsheets during accelerated aging.

3.3 | Exposure Effects on Physical Material Properties

Our previous study of exposed PP-based backsheet surfaces suggested erosion of the air side with accelerated environmental aging [18], which has also been reported in other studies of polyolefin-based co-extruded backsheets [35]. To further investigate this, the cross-sectioned layer thicknesses of exposed backsheets were measured using LCSM. As shown in Figure 5, the exposed air side layer thickness decreased 16% to 22% with initial 30-day exposure for all exposure conditions, then remained constant at this reduced thickness for additional exposure time. This initial decrease may be due to molecular ordering as a result of postcrystallization where accelerated aging between the glass transition temperature, T_g (approximately −20°C to 20°C for isotactic PP), and the melting temperature, T_m (approximately 166°C measured using DSC), for prolonged times, can allow for reordering of the molecular chains through the release and rearrangement of physical bonds along with relaxation of entangled molecular chains, reducing the free volume [16, 36]. The plateaued behavior with longer exposure time indicates that the added pigments protect the backsheet from further degradation, especially in the core layer. The core- and cell-side layer thicknesses are not reported due to the high variation produced by the surface roughness of the cell side layer.

Crystallinity has been identified as an important early indicator of embrittlement and failure in PV backsheets [8, 9]. The crystallinity results measured using DSC are summarized in

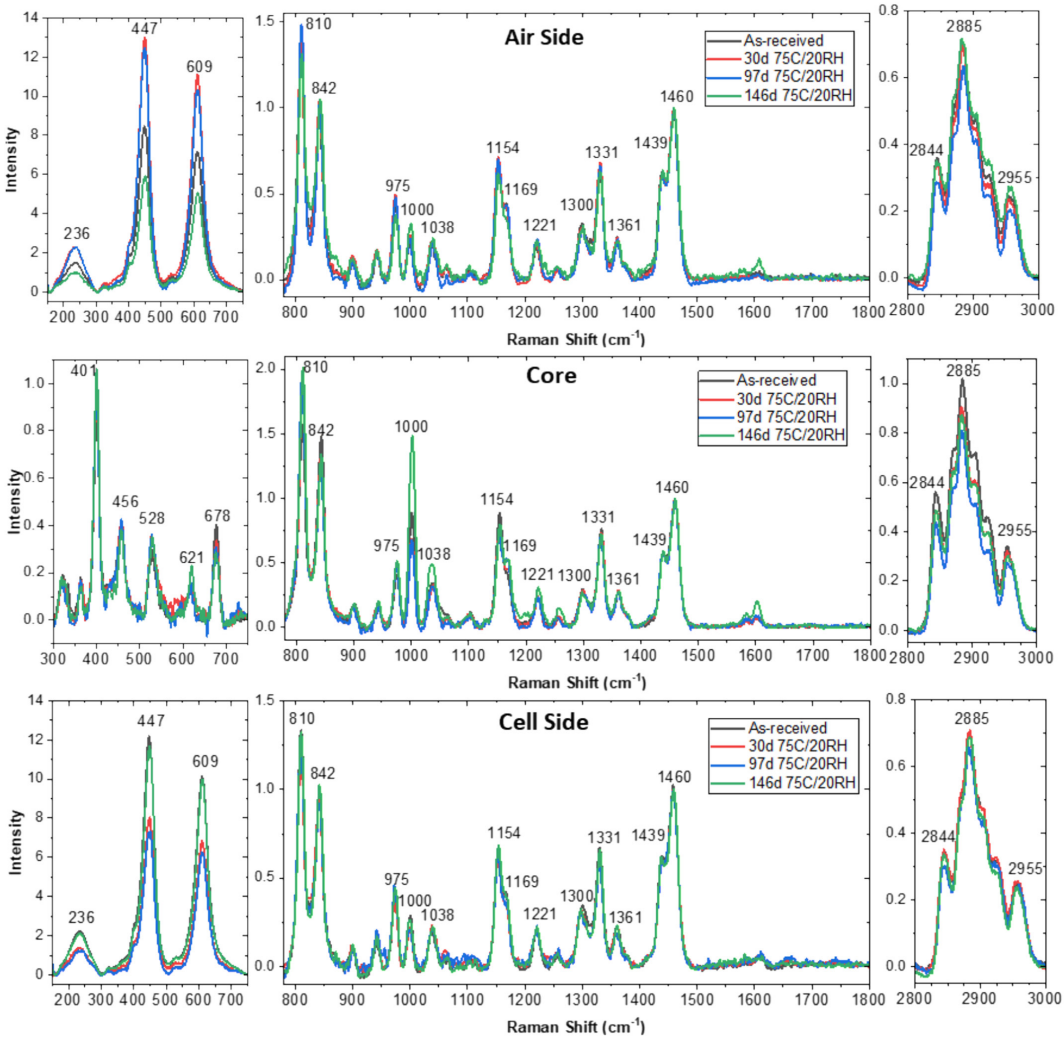

FIGURE 3 | Representative Raman spectra comparison of air-side, core, and cell-side layers in PP-based backsheets exposed to UV at 75°C/20% RH for variable duration. Spectra are normalized to the 1460 cm^{-1} peak. [Color figure can be viewed at wileyonlinelibrary.com]

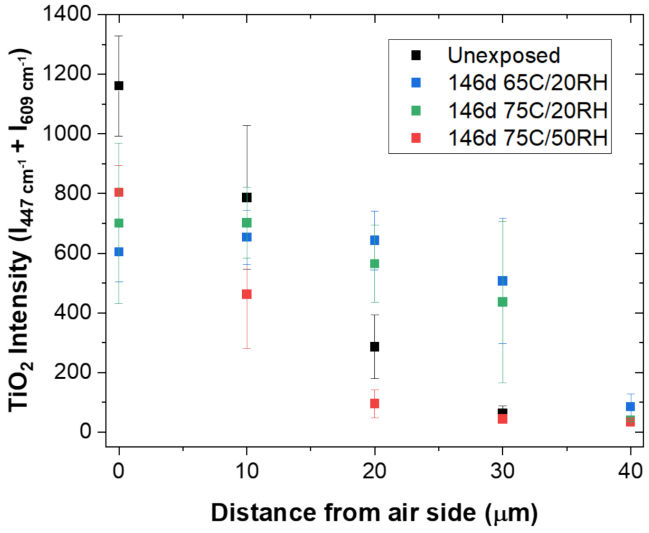

FIGURE 4 | Spatially resolved average TiO_2 intensity measured by Raman spectroscopy of PP backsheets unexposed and aged for 146 days at 65°C/20% RH, 75°C/20% RH, and 75°C/50% RH. TiO_2 intensity is calculated as the sum of the integrated peak area of the 447 and 609 cm^{-1} TiO_2 Raman peaks. Reported error is the standard deviation of five measurements. [Color figure can be viewed at wileyonlinelibrary.com]

Figure 6. Samples aged at 65°C/20% RH and 75°C/50% RH did not result in statistically significant changes with exposure time. In the case of samples aged at 75°C/20% RH, the crystallinity increased gradually with exposure by 3.2% after 146 days. Other accelerated aging studies of PP-based backsheets have similarly reported no significant changes in the thermal properties with exposure [7, 16]. However, it is important to note that this is a bulk measurement that cannot resolve individual components or heterogeneous changes within the sample. This is a crucial requirement for multilayered composite structures, which is why Raman spectroscopy was also used to measure the effect of accelerated aging on crystallinity.

A Raman microscope was used to measure heterogeneous PP crystallinity across the PP backsheet cross-sections (Figure 7a,c,e). A significant increase in crystallinity is observed in the core layers after 30-day exposure for all tested conditions, indicating a postcrystallization process due to aging. The trends in postcrystallization are in agreement with the reduced film thicknesses measured after accelerated aging (Figure 5), which were attributed to postcrystallization. This process generally stabilized after 30 days. For the 65°C/20% RH and 75°C/20% RH samples, a small additional increase in crystallinity in the core layer was measured after 97-day exposure with no change after

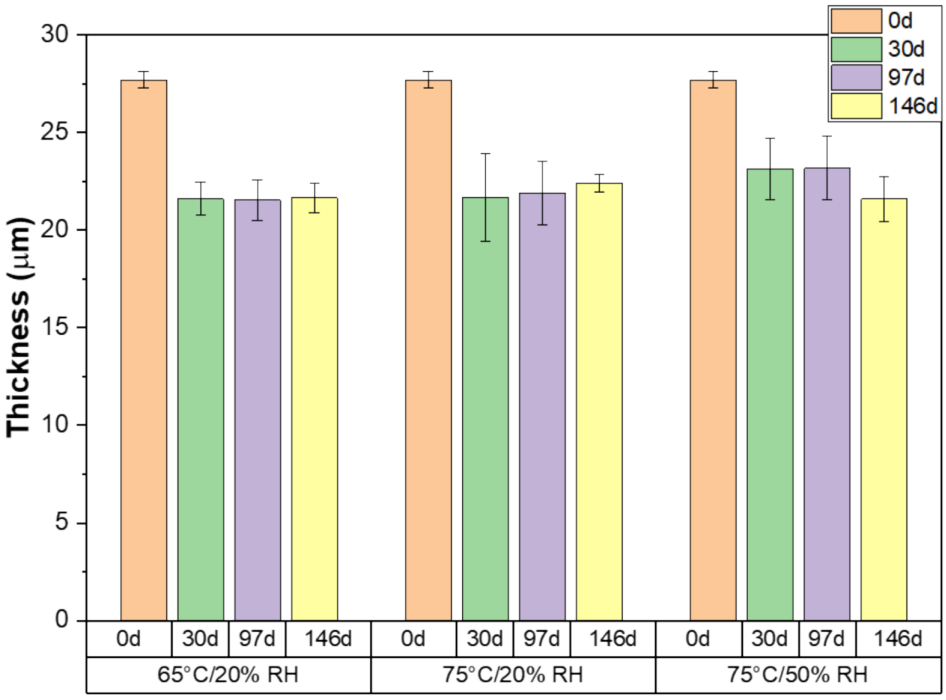

FIGURE 5 | Thickness measurements of air-side layer in exposed PP backsheets. Error is the standard deviation of four measurements. [Color figure can be viewed at wileyonlinelibrary.com]

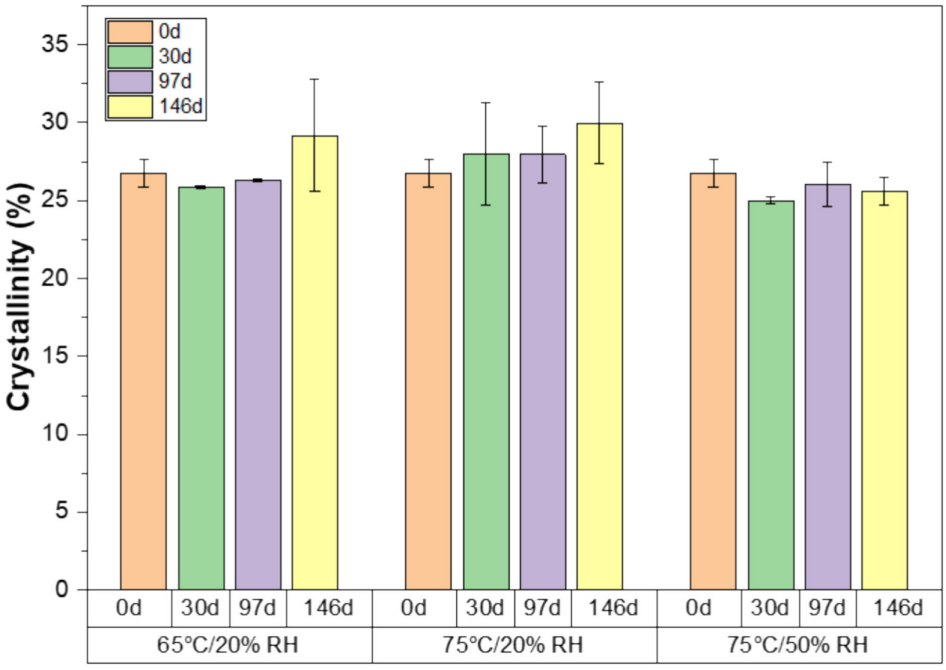

FIGURE 6 | Exposure effects on PP backsheet crystallinity measured using DSC. Error is the standard deviation of three measurements. [Color figure can be viewed at wileyonlinelibrary.com]

146 days. In the case of 75°C/50% RH, the crystallinity was more stable after the initial 30-day increase compared with the other exposure conditions, although a slight increase was observed after 97 days, followed by a decrease in crystallinity after 147-day exposure. These conditions may have resulted in the fastest postcrystallization rate due to the increased humidity, likely due to the ability of water to act as a plasticizer and increase the mobility of the polymer chains, promoting faster crystallization. Hydrophilic additives such as TiO_2 may also increase water diffusion through the backsheet to the core layer, further facilitating this process.

A large distribution was measured in the air- and back-side layers, which is likely due to heterogeneity within the layers due to additives, such as TiO_2. Overall, these layers appeared generally stable throughout aging. The air-side crystallinity was

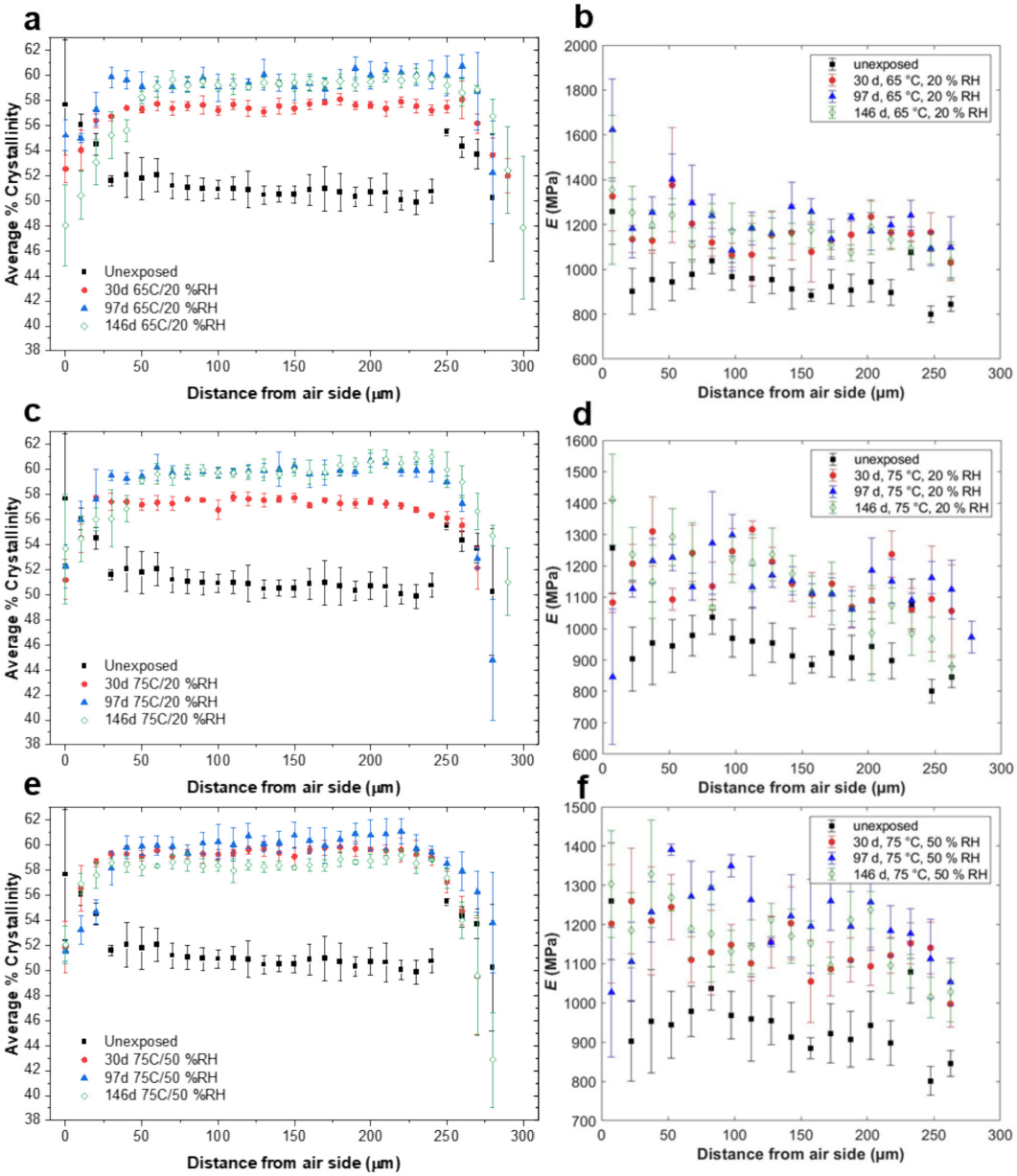

FIGURE 7 | Spatially resolved (a, c, e) crystallinity measured by Raman spectroscopy and (b, d, f) Young's modulus (E) of PP backsheets aged at (a, b) 65°C/20% RH, (c, d) 75°C/20% RH, and (e, f) 75°C/50% RH for variable duration. For the nanoindentation results, each point is the average measured Young's modulus of all indents within a 15-μm interval (four to nine indents, with the exception of the cell side layer, where only two to four indents were available due to its high surface roughness). Reported error for crystallinity is the standard deviation of five measurements. Reported error for nanoindentation is the standard deviation calculated from the indents within the specified range and the individual depth-modulus curves. [Color figure can be viewed at wileyonlinelibrary.com]

somewhat reduced with aging, but the large standard deviation in these layers prevented the identification of any clear trend with increasing exposure time. Stability in the outer layers is unsurprising, however, due to the inclusion of TiO_2, a known stabilizer in other backsheet materials through the suppression of hydroperoxide formation and protection from UV-radiation penetration [36, 37]. Synchrotron-based microfocused WAXS was used to validate this method. Figure 8 shows the integrated intensity of the crystalline (110) PP peak at 2.02 $Å^{-1}$ across the sample surface where the core layer crystallinity increases after 30 days of accelerated aging at 75°C/50% RH. Although additional measurements are required, including repeat measurements, these preliminary data are in strong agreement with the overall trend seen in the crystallinity measured using Raman spectroscopy.

Since crystallinity influences many performance parameters in PV backsheets [8, 9], including the mechanical properties; these spatially resolved crystallinity measurements were compared with Young's modulus using nanoindentation over the cross-sectioned samples (Figure 7b,d,f). The trends identified in the crystallinity measured using Raman spectroscopy are generally in agreement with those seen in the nanoindentation where the modulus increases in the core layer within the first 30 days of exposure, followed by subsequent stabilization. The overall trend in the unexposed sample is similarly consistent with the crystallinity

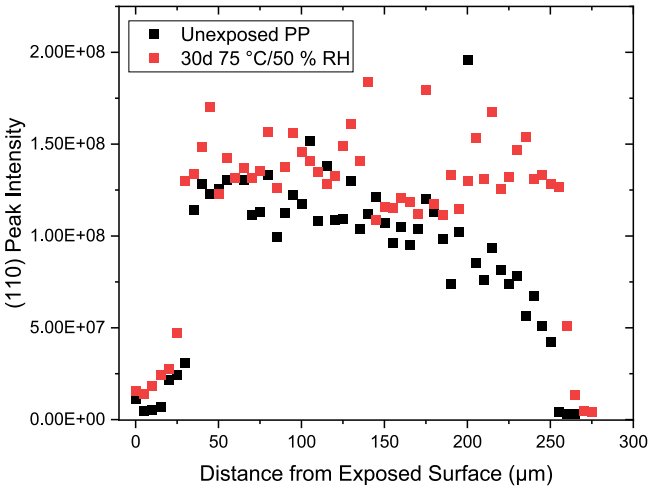

FIGURE 8 | Integrated peak intensity of the crystalline (110) PP peak at 2.02 $Å^{-1}$ measured using synchrotron-based microfocused WAXS across the cross-sectioned backsheet. [Color figure can be viewed at wileyonlinelibrary.com]

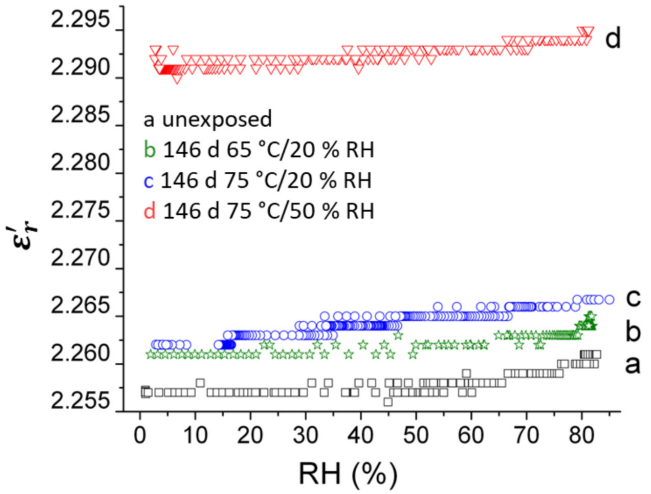

FIGURE 9 | The real part of the dielectric permittivity, ε_r', measured for PP-based backsheets as a function of RH after accelerated aging under the following environmental conditions: (a) unexposed (black squares), (b) 146 days 65°C/20% RH (green stars), (c) 146 days 75°C/20% RH (blue circles), and (d) 146 days 75°C/50% RH (red triangles). The relative uncertainty of individual ε_r' data is 1.3×10^{-3}. The apparent scattering of data points results from uncertainty in RH measurements. [Color figure can be viewed at wileyonlinelibrary.com]

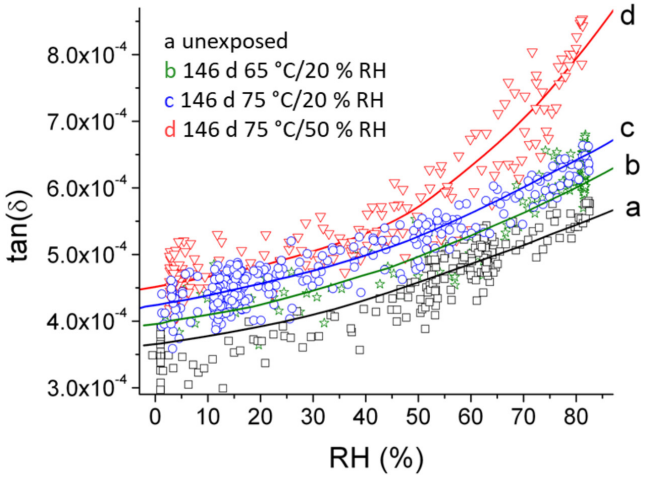

FIGURE 10 | The dielectric loss, tan(δ), measured for PP-based backsheets as a function of RH after accelerated aging under the following environmental conditions: (a) unexposed (black squares), (b) 146 days 65°C/20% RH (green stars), (c) 146 days 75°C/20% RH (blue circles), and (d) 146 days 75°C/50% RH (red triangles). The symbols represent the data points, and the lines are fitting results to an arbitrary function to guide the eye. The combined uncertainty of the individual ε_r' data is 1×10^{-4}. [Color figure can be viewed at wileyonlinelibrary.com]

measurements, supporting the validity of this method of assessing heterogeneous crystallinity in multilayered backsheets. The large variation in the modulus is attributable to sample heterogeneity, most likely due to additive inclusions. No delamination was observed in the exposed samples, which is in agreement with other studies of co-extruded PP-based backsheets [17].

3.4 | Dielectric Performance Properties

The dielectric characterization of 146-day exposed backsheets showed a small decrease in performance with aging, further indicating the advantage of spatially resolved crystallinity measured using Raman spectroscopy. This effect is most pronounced for the backsheet aged at 75°C/50% RH. Figure 9 shows the real part of the dielectric permittivity, ε_r', measured as a function of RH for PP-based backsheet samples unexposed and exposed to accelerated aging. It is seen that ε_r' of all tested samples increases by a small amount of about 3×10^{-3} with increasing RH from 2% to 85%, due to uptake of water, $\varepsilon'_{\text{r-H2O}}\approx78$. Also, ε_r' of backsheets aged at 65°C/20% RH and 75°C/20% RH is larger by approximately 0.006 compared to the as-received backsheet. In comparison, ε_r' is significantly larger, by approximately 0.04, indicating possible parament alteration of the chemical composition resulting from increased humidity.

Figure 10 shows the effect of RH on the dielectric loss tangent ($\tan(\delta)=\varepsilon_r''/\varepsilon_r'$), which is directly proportional to conductivity but independent of the specimen dimensions. Such notation minimizes possible systematic uncertainty from the specimens' dimensional imperfections. The measured dielectric loss increases substantially within the RH range between 40% and 85% after accelerated aging (Figure 10). The difference between tan(δ) of UV-exposed PV backsheets versus tan(δ) of the unexposed backsheet approaches 4×10^{-4} at RH above 85%. This increase in tan(δ) may arise from hydrophilic UV-generated ionic surface decomposition byproducts that bind additional water molecules and increase water mobility (i.e., electrical conductivity) even at high microwave frequencies. This includes the increased surface hydrophilicity that occurs with photo-oxidation of PP [37]. This effect may accelerate with environmental aging that leads to an increase of UV absorption and was most pronounced for aging at 75°C/50% RH, also indicating moisture sensitivity during aging. Nevertheless, regarding the insulation resistance, the observed increase in the dielectric loss is not significant though tends to accelerate, especially in higher humidity environment, which may be correlated with faster postcrystallization. Further measurements are required to evaluate these findings from

a reliability perspective and to determine if a correlative relationship can be obtained between dielectric and independent measurements, as well as improved modeling studies to validate insulation degradation mechanisms considering these data.

4 | Conclusion

This study investigated accelerated aging effects on the material properties of PP-based backsheets and established new applications of Raman spectroscopy for the evaluation of PV backsheet degradation. The backsheets are comprised of a three-layered co-extruded structure where the outer layers are $\approx 27\,\mu m$ and the core layer is $\approx 224\,\mu m$. Spatially resolved material characterization was used to assess aging-related heterogeneous material property changes. Crystallinity was measured as an early failure indicator. Although previous studies of these materials have shown stable crystallinity [7], spatially resolved crystallinity measurements using Raman spectroscopy and microfocused WAXS showed increased crystallinity in the core layer attributed to heterogeneous postcrystallization with environmental aging. The Raman data indicated that postcrystallization may be accelerated by high humidity conditions. Spatially resolved nanoindentation measured increased modulus in the core layer, consistent with the trends measured in crystallinity. These results, combined with the small reduction in insulative performance measured using dielectric characterization, support the use of crystallinity as an early failure indicator for PV backsheets.

Although some heterogeneous material property changes were measured, these shifts generally stabilized with additional accelerated aging. Thus, while some embrittlement and reduced insulative performance may occur in the core layer as a result of postcrystallization, this effect may be minimal. The dielectric characterization results showed reduced performance with increased RH and overall reduced performance for sampled aged under high RH conditions. Combined with the crystallinity trends observed using Raman spectroscopy, this result suggests that the material properties of these backsheets may be most sensitive to moisture as an environmental stressor. Overall, our study indicates that co-extruded PP-based backsheets show general stability during accelerated aging, although additional tests are needed to confirm their long-term performance, especially regarding potential interfacial interactions when integrated into PV modules.

Author Contributions

Ashlee Aiello: writing – original draft, Raman spectroscopy, DSC, WAXS methodology, investigation, data analysis, visualization. **Stefan Mitterhofer:** writing – original draft, review, and editing, nanoindentation methodology, investigation, data analysis, visualization. **Jan Obrzut:** writing – original draft, review, and editing, dielectric methodology, data analysis, visualization. **Karissa L. Jensen:** writing – review and editing, sample preparation, SPHERE methodology, UV spectra data collection. **Patryk Wąsik:** writing – review and editing, WAXS operation, methodology, data analysis, visualization. **Chiara Barretta:** writing – review and editing, resources. **Gernot Oreski:** writing – review and editing, resources. **Stephanie S. Watson:** writing – review and editing, resources. **Lipiin Sung:** writing – review and editing, resources. **Xiaohong Gu:** writing – review and editing, resources, project administration, methodology, conceptualization.

Acknowledgments

This research used the Soft Matter Interfaces 12-ID beamline of the National Synchrotron Light Source II, a US Department of Energy (DOE) Office of Science User Facility operated for the DOE Office of Science by Brookhaven National Laboratory under contract no. DE-SC0012704.

Conflicts of Interest

The authors declare no conflicts of interest.

Data Availability Statement

The data that support the findings of this study are available from the corresponding author upon reasonable request.

References

1. Y. Lyu, A. Fairbrother, M. Gong, et al., "Drivers for the Cracking of Multilayer Polyamide-Based Backsheets in Field Photovoltaic Modules: In-Depth Degradation Mapping Analysis," *Progress in Photovoltaics: Research and Applications* 28, no. 7 (2020): 704–716, https://doi.org/10.1002/pip.3260.

2. Y. Lyu, J. H. Kim, A. Fairbrother, and X. Gu, "Degradation and Cracking Behavior of Polyamide-Based Backsheet Subjected to Sequential Fragmentation Test," *IEEE Journal of Photovoltaics* 8, no. 6 (2018): 1748–1753, https://doi.org/10.1109/jphotov.2018.2863789.

3. M. D. Kempe, T. Lockman, and J. Morse, "Development of Testing Methods to Predict Cracking in Photovoltaic Backsheets," in *2019 IEEE 46th Photovoltaic Specialists Conference (PVSC)* (Chicago, IL: IEEE, 2019): 2411–2416, https://doi.org/10.1109/PVSC40753.2019.8980818.

4. W. Gambogi, et al., "A Comparison of Key PV Backsheet and Module Performance From Fielded Module Exposures and Accelerated Tests," *IEEE Journal of Photovoltaics* 4, no. 3 (2014): 935–941, https://doi.org/10.1109/jphotov.2014.2305472.

5. G. C. Eder, Y. Voronko, G. Oreski, et al., "Error Analysis of Aged Modules With Cracked Polyamide Backsheets," *Solar Energy Materials & Solar Cells* 203 (2019): 110194, https://doi.org/10.1016/j.solmat.2019.110194.

6. G. Oreski, N. P. Dasgupta, X. Meng, J. W. Elam, and A. B. Martinson, "Atomic Layer Deposition of Metal Sulfide Materials," *Accounts of Chemical Research* 48, no. 2 (2015): 341–348, https://doi.org/10.1088/2516-1083/ac6f3f.

7. G. Oreski, C. Barretta, A. Macher, et al., "Investigation of the Crack Propensity of Co-Extruded Polypropylene Backsheet Films for Photovoltaic Modules," *Solar Energy Materials & Solar Cells* 259 (2023): 112438, https://doi.org/10.1016/j.solmat.2023.112438.

8. M. Aghaei, A. Fairbrother, A. Gok, et al., "Review of Degradation and Failure Phenomena in Photovoltaic Modules," *Renewable and Sustainable Energy Reviews* 159 (2022): 112160, https://doi.org/10.1016/j.rser.2022.112160.

9. G. Oreski and G. M. Wallner, "Aging Mechanisms of Polymeric Films for PV Encapsulation," *Solar Energy* 79, no. 6 (2005): 612–617, https://doi.org/10.1016/j.solener.2005.02.008.

10. C. Peike, T. Kaltenbach, K. A. Weiß, and M. Koehl Indoor Vs. Outdoor Aging: Polymer Degradation in PV Modules Investigated by Raman Spectroscopy, presented at the Reliability of Photovoltaic Cells, Modules, Components, and Systems V, 2012.

11. C. Peike, T. Kaltenbach, M. Köhl, and K. A. Weiß, "Lateral Distribution of the Degradation of Encapsulants After Different Damp-Heat Exposure Times Investigated by Raman Spectroscopy," in *Reliability of Photovoltaic Cells, Modules, Components, and Systems III*, Vol. 7773 (SPIE, 2010).

12. C. Peike, T. Kaltenbach, K. A. Weiß, and M. Koehl, "Non-Destructive Degradation Analysis of Encapsulants in PV Modules by Raman Spectroscopy," *Solar Energy Materials & Solar Cells* 95, no. 7 (2011): 1686–1693, https://doi.org/10.1016/j.solmat.2011.01.030.

13. K. J. Geretschläger, G. M. Wallner, and J. Fischer, "Structure and Basic Properties of Photovoltaic Module Backsheet Films," *Solar Energy Materials & Solar Cells* 144 (2016): 451–456, https://doi.org/10.1016/j.solmat.2015.09.060.

14. O. Stroyuk, C. Buerhop-Lutz, A. Vetter, J. Hauch, and C. J. Brabec, "Nondestructive Characterization of Polymeric Components of Silicon Solar Modules by Near-Infrared Absorption Spectroscopy (NIRA)," *Solar Energy Materials & Solar Cells* 216 (2020): 110702, https://doi.org/10.1016/j.solmat.2020.110702.

15. C.-C. Lin, P. J. Krommenhoek, S. S. Watson, and X. Gu, "Depth Profiling of Degradation of Multilayer Photovoltaic Backsheets After Accelerated Laboratory Weathering: Cross-Sectional Raman Imaging," *Solar Energy Materials & Solar Cells* 144 (2016): 289–299, https://doi.org/10.1016/j.solmat.2015.09.021.

16. A. Omazic, G. Oreski, M. Edler, et al., "Increased Reliability of Modified Polyolefin Backsheet Over Commonly Used Polyester Backsheets for Crystalline PV Modules," *Journal of Applied Polymer Science* 137, no. 30 (2020): 48899, https://doi.org/10.1002/app.48899.

17. G. Oreski, G. C. Eder, Y. Voronko, et al., "Performance of PV Modules Using Co-Extruded Backsheets Based on Polypropylene," *Solar Energy Materials & Solar Cells* 223 (2021): 110976, https://doi.org/10.1016/j.solmat.2021.110976.

18. K. L. Jensen, A. Aiello, S. Mitterhofer, et al., "Surface Photooxidation of Polypropylene-Based Photovoltaic Backsheets: A Comprehensive Spectroscopic Investigation," *Polymer Degradation and Stability* 232 (2025): 111132, https://doi.org/10.1016/j.polymdegradstab.2024.111132.

19. N. D. Orloff, J. Obrzut, C. J. Long, et al., "Dielectric Characterization by Microwave Cavity Perturbation Corrected for Nonuniform Fields," *IEEE Transactions on Microwave Theory and Techniques* 62, no. 9 (2014): 2149–2159, https://doi.org/10.1109/tmtt.2014.2336775.

20. S. Seethamraju, J. Obrzut, J. F. Douglas, J. W. Woodcock, and J. W. Gilman, "Quantifying Fluorogenic Dye Hydration in an Epoxy Resin by Noncontact Microwave Dielectric Spectroscopy," *Journal of Physical Chemistry. B* 124, no. 14 (2020): 2914–2919, https://doi.org/10.1021/acs.jpcb.9b11622.

21. J. Obrzut, J. A. Clark, A. E. Baumann, and J. F. Douglas, "Dielectric Characterization of H(2)O and CO(2) Uptake by Polyethylenimine Films," *Langmuir* 40, no. 16 (2024): 8562–8567, https://doi.org/10.1021/acs.langmuir.4c00247.

22. J. Chin, E. Byrd, N. Embree, et al., "Accelerated UV Weathering Device Based on Integrating Sphere Technology," *Review of Scientific Instruments* 75, no. 11 (2004): 4951–4959, https://doi.org/10.1063/1.1808916.

23. 2024. *DuraMAT FY 2023 Annual Report: Toward Reliability Forecasting*. Research Organization: National Renewable Energy Laboratory (NREL), Golden, CO (United States) Sponsoring Organization: USDOE Office of Energy Efficiency and Renewable Energy (EERE), Renewable Power Office. Solar Energy Technologies Office [Online] Available: https://www.osti.gov/biblio/2319198.

24. A. S. Nielsen, D. N. Batchelder, and R. Pyrz, "Estimation of Crystallinity of Isotactic Polypropylene Using Raman Spectroscopy," *Polymer* 43 (2002): 2671–2676.

25. X. Li and B. Bhushan, "A Review of Nanoindentation Continuous Stiffness Measurement Technique and Its Applications," *Materials Characterization* 48, no. 1 (2002): 11–36.

26. S. Mitterhofer, S. Smith, A. Aiello, K. Jensen, and X. Gu, *Investigating PV Module Packaging Mechanical Properties With Cross-Sectional Nano-Indentation, in EUPVSEC* (Vienna, 2024).

27. Y. Liu, B. Cheng, K. K. Wang, et al., "Study of Raman Spectra for γ-Al2O3 Models by Using First-Principles Method," *Solid State Communications* 178 (2014): 16–22, https://doi.org/10.1016/j.ssc.2013.09.030.

28. J. Zhang, M. Li, Z. Feng, J. Chen, and C. Li, "UV Raman Spectroscopic Study on TiO2. I. Phase Transformation at the Surface and in the Bulk," *Journal of Physical Chemistry. B* 110 (2006): 927–935.

29. U. Balachandran and N. G. Eror, "Raman Spectra of Titanium Dioxide," *Journal of Solid State Chemistry* 42 (1982): 276–282.

30. S. P. S. Porto, P. A. Fleury, and T. C. Damen, "Raman Spectra of TiO2, MgF2, ZnF2, FeF2, and MnF2," *Physical Review* 154, no. 2 (1967): 522–526, https://doi.org/10.1103/PhysRev.154.522.

31. M. Kaizuka, H. Sato, Y. Ozaki, and H. Sato, "Visualization of Recrystallization Induced by Ultraviolet Degradation of a Polypropylene Film Using Raman Imaging," *Applied Spectroscopy* 78, no. 5 (2024): 517–522, https://doi.org/10.1177/00037028241235233.

32. H. Tadokoro, M. Kobayashi, M. Ukita, K. Yasufuku, S. Murahashi, and T. Torii, "Normal Vibrations of the Polymer Molecules of Helical Conformation. V. Isotactic Polypropylene and Its Deuteroderivatives," *Journal of Chemical Physics* 42, no. 4 (1965): 1432–1449, https://doi.org/10.1063/1.1696134.

33. R. G. Snyder and J. H. Schachtschneider, "Valence Force Calculation of the Vibrational Spectra of Crystalline Isotactic Poypropylene and Some Deuterated Polypropylenes," *Spectrochimica Acta* 20, no. 5 (1963): 853–869.

34. T. Kida, Y. Hiejima, and K. H. Nitta, "Rheo-Raman Study of Isotactic Polypropylene Under Tensile Deformation," *Macromolecular Symposia* 377, no. 1 (2018): 1700019, https://doi.org/10.1002/masy.201700019.

35. M. Thuis, N. M. Al Hasan, R. L. Arnold, B. King, and A. Maes, "A Comparison of Emerging Nonfluoropolymer-Based Coextruded PV Backsheets to Industry-Benchmark Technologies," *IEEE Journal of Photovoltaics* 12, no. 1 (2022): 88–96, https://doi.org/10.1109/jphotov.2021.3117915.

36. A. Omazic, G. Oreski, M. Halwachs, et al., "Relation Between Degradation of Polymeric Components in Crystalline Silicon PV Module and Climatic Conditions: A Literature Review," *Solar Energy Materials & Solar Cells* 192 (2019): 123–133, https://doi.org/10.1016/j.solmat.2018.12.027.

37. G. Grause, M.-F. Chien, and C. Inoue, "Changes During the Weathering of Polyolefins," *Polymer Degradation and Stability* 181 (2020): 109364, https://doi.org/10.1016/j.polymdegradstab.2020.109364.

Supporting Information

Additional supporting information can be found online in the Supporting Information section.